

## Supplementary Information for

### **Self-induced interface enhanced moisture-harvesting and light-trapping toward high performance electric power generation**

Jiixin Bai<sup>a</sup>, Qihua Liao<sup>a</sup>, Houze Yao<sup>a</sup>, Tianlei Guang<sup>a</sup>, Tiancheng He<sup>a</sup>, Huhu Cheng<sup>ab</sup>  
and Liangti Qu<sup>\*ab</sup>

<sup>a</sup>Laboratory of Flexible Electronics Technology, Key Laboratory of Organic Optoelectronics & Molecular Engineering, Ministry of Education, Department of Chemistry, Tsinghua University, Beijing, 100084, China.

<sup>b</sup>State Key Laboratory of Tribology in Advanced Equipment, Department of Mechanical Engineering, Tsinghua University, Beijing, 100084, China.

E-mail: [lqu@mail.tsinghua.edu.cn](mailto:lqu@mail.tsinghua.edu.cn)

#### **This supplementary information file includes:**

Figs. S1 to S36  
Tables S1 to S5

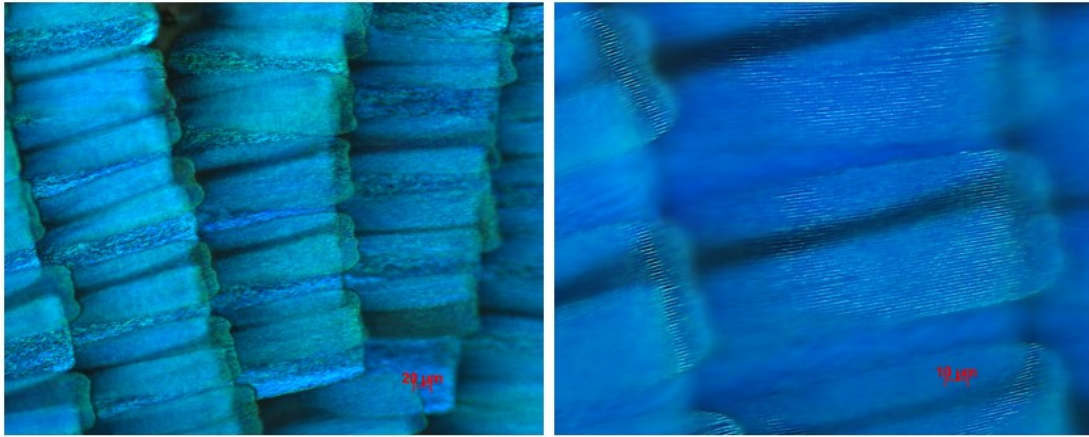


Fig. S1 Microscopic images of *Papilio paris*.

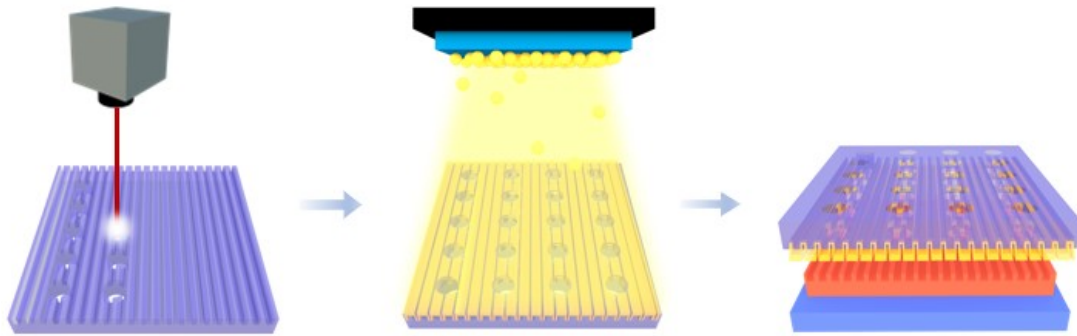


Fig. S2 Porous DVD manufactured by laser (355 nm UV) processing. Vacuum sputtering of AuNPs on porous DVD to build a ME. Stacking electrodes and PSSA-Kc film for an IEG.

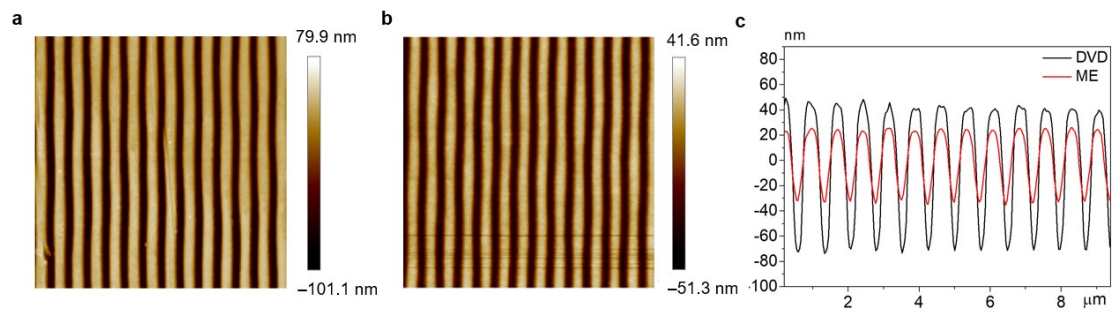


Fig. S3 AFM images of an original DVD and ME.

Such sinusoidal morphology is retained well after manufacturing holes and coating AuNPs.

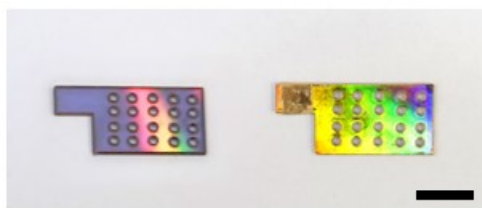


Fig. S4 The photographs of porous DVD and ME. Scale bar: 1 cm.

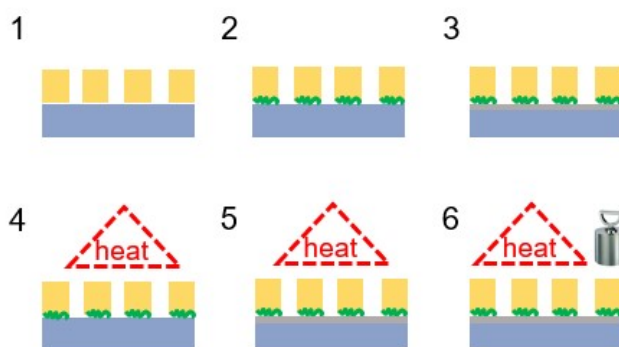


Fig. S5 Illustration of different contact modes between top electrode and PSSA-Kc film. (1) Planar electrode touching with film. (2) ME touching with film. (3) ME touching with film after moisture adsorption. (4) ME touching with film and annealing. (5) ME touching with film after moisture adsorption and annealing. (6) ME touching with film after moisture adsorption and annealing, pressing.

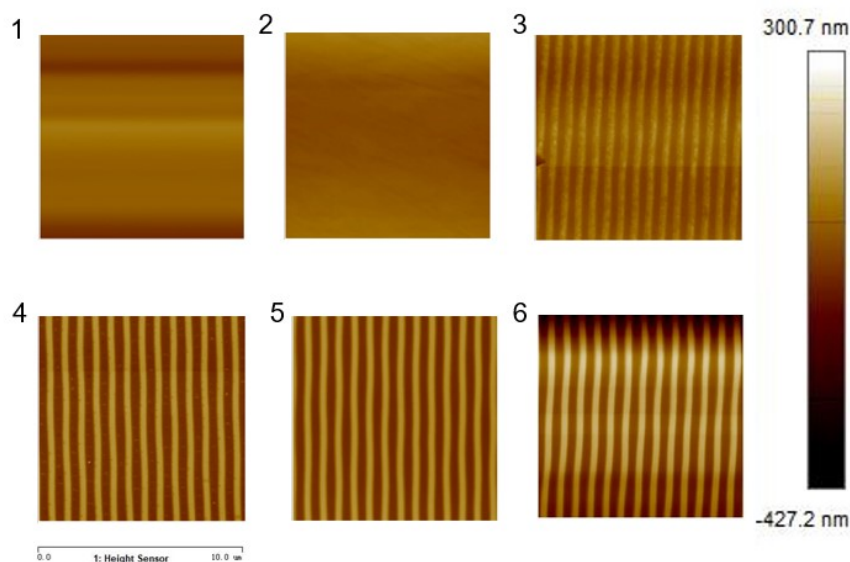


Fig. S6 AFM images of *i*-PSSA-Kc film after different contact modes with electrode. (1) Planar electrode touching with film. (2) ME touching with film. (3) ME touching with film after moisture adsorption. (4) ME touching with film and annealing. (5) ME touching with film after moisture adsorption and annealing. (6) ME touching with film after moisture adsorption and annealing, pressing.

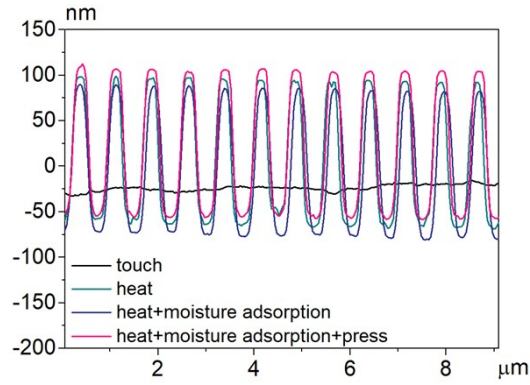


Fig. S7 The corresponding height analysis of different contact modes in AFM images of Fig. S6.

As shown in Fig. S5–S7, the depth of microgroove in i-PSSA-Kc film will be deepened after annealing or press IEG, which means that self-induced imprinting process by moisture adsorption will not result in PSSA-Kc gel to fill in the grooves of ME absolutely. There is still space for further water migration.

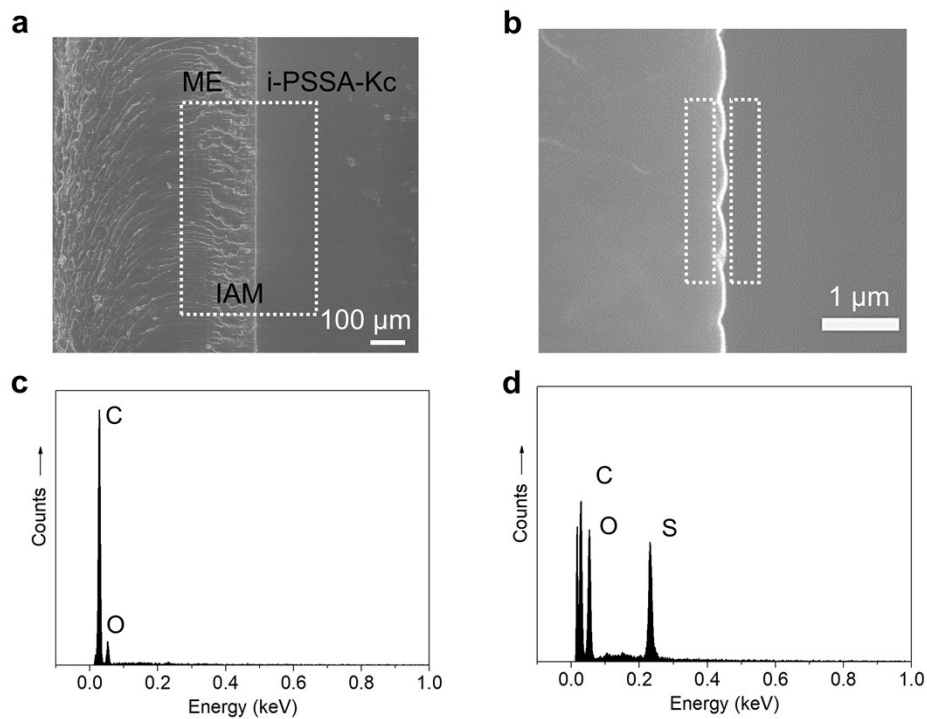


Fig. S8 (a), (b) The cross-sectional SEM image of the interface between ME and i-PSSA-Kc film. Energy disperse spectrogram of regions in (c) ME and (d) i-PSSA-Kc film, respectively. The scanned area are white boxes in (b).

Table S1 The relative percentages (at%) from energy dispersive X-ray spectrum of regions in ME and i-PSSA-Kc film.

	ME	i-PSSA-Kc
<b>C</b>	71.78	46.56
<b>N</b>	28.22	41.34
<b>S</b>		11.10

\*The scanned area are white boxes in Fig. S8b

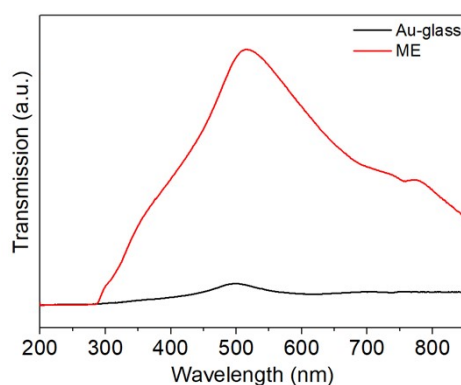


Fig. S9 Transmission spectra of ME and AuNPs coated glass.

In a ME, the AuNPs coated on the ME is not only responsible for conduction, but strengthen the surface electromagnetic field due to surface plasmon resonance effect,<sup>1</sup> which contributes to ME with high transmittance comparing to planar electrode.

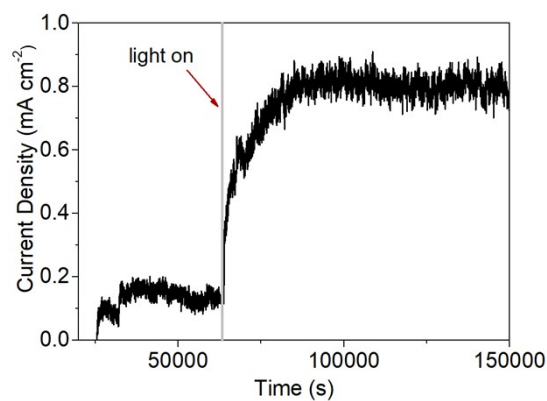


Fig. S10  $I_{sc}$  output of IEG under only moisture further enhancing after illumination.

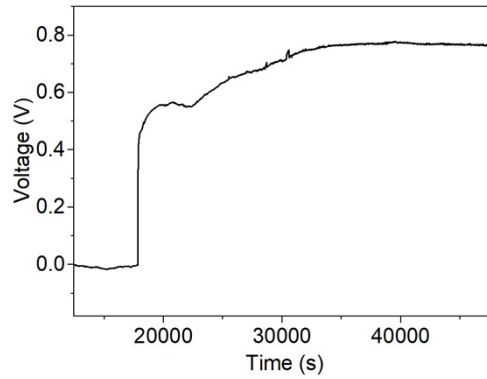


Fig. S11  $V_{oc}$  output of IEG under constant RH of 70%, and light intensity of  $100 \text{ mW cm}^{-2}$ .

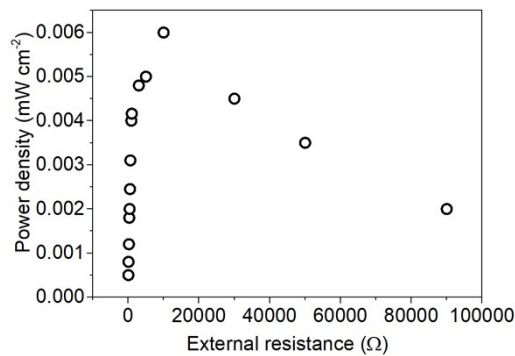


Fig. S12 Electric output of IEG with different electrical resistance as load under RH = 70%.

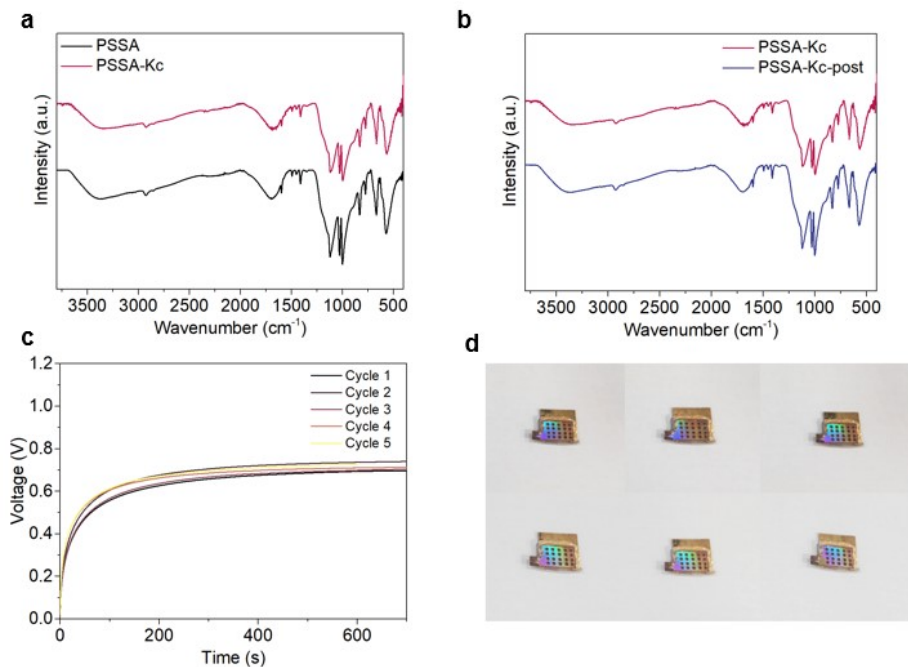


Fig. S13 FTIR curves of (a) PSSA and PSSA-Kc film, (b) FTIR curves of PSSA-Kc film before and after cycling performance test. They show identical profile, indicating no functional group changing during the test. (c) Repeatable power generation of an IEG. (d) Photographs of IEG before and after cycling performance test. The device was dried for 12 hours after every cycle.

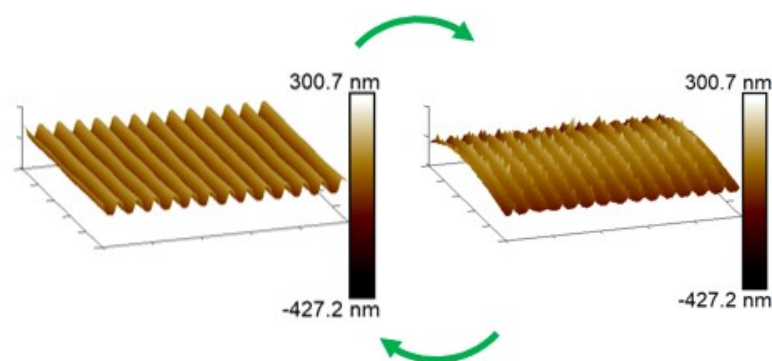


Fig. S14 AFM images of i-PSSA-Kc film before and after cycling performance test.

The functional groups in i-PSSA-Kc film will not be destroyed during cycling test and the microstructure in the interface can be rebuilt after water absorption and desorption, which result in reversibility of electricity generation in IEG.

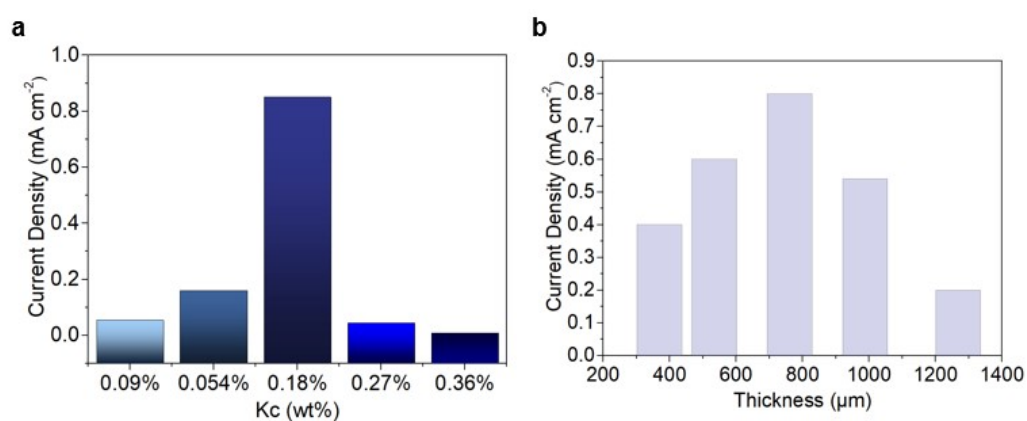


Fig. S15 (a) The dependence of  $I_{sc}$  on different content (wt%) of Kc in i-PSSA-Kc film. (b)  $I_{sc}$  of IEG based on i-PSSA-Kc film with different film thickness.

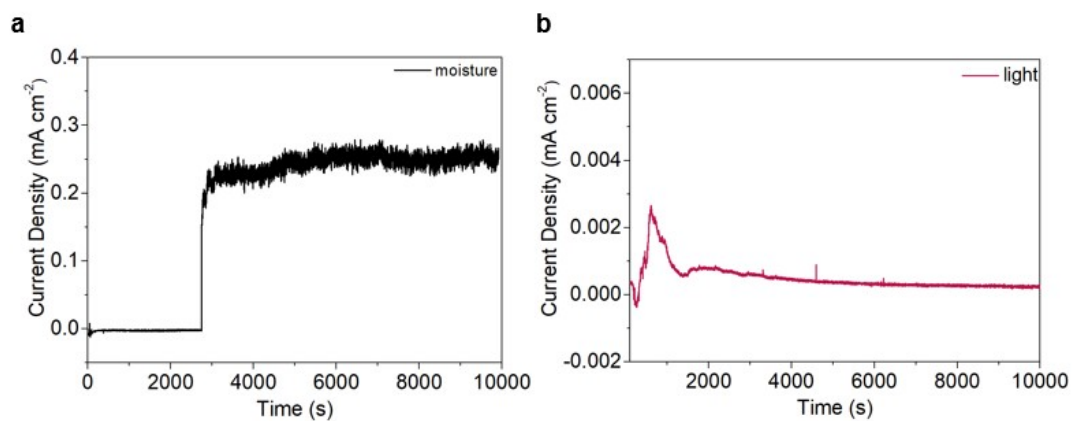


Fig. S16  $I_{sc}$  output of a IEG under (a) RH of 70%, (b) light intensity of  $100 \text{ mW cm}^{-2}$ , respectively.

The IEG can work well at simple or dual-drive mode under moisture or light to achieve power output.

The  $I_{sc}$  reaches a maximum value of  $0.25 \text{ mA cm}^{-2}$  upon moisture incoming solely, which is higher than the reported MEGs.<sup>2,3</sup> When light illuminates the sample in the absence of moisture, the instantaneous photocurrent occurs, followed by decline near to zero, which suggests the recombination of photogenerated carriers.<sup>4</sup> Remarkably, the electric output of IEG under moisture and light simultaneously is much higher and more stable than the performance induced by single source.

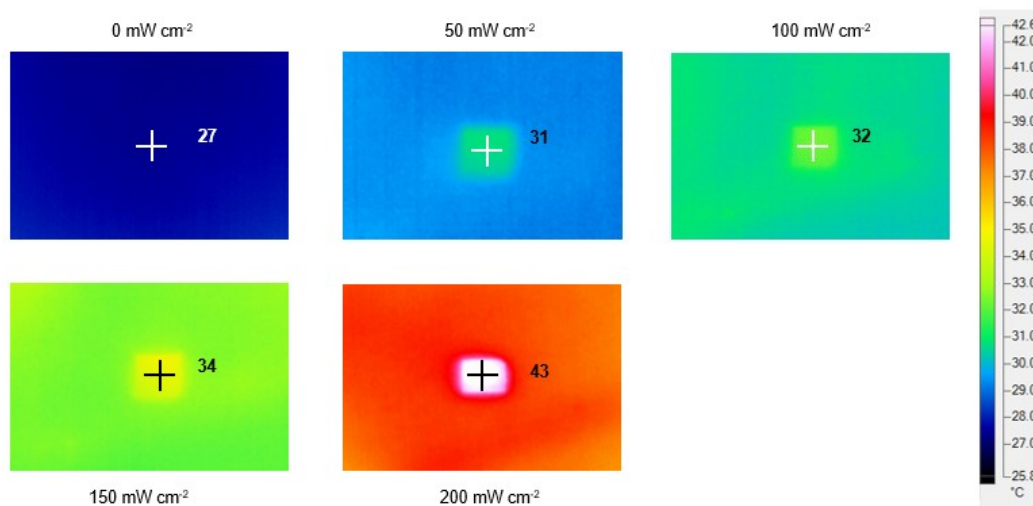


Fig. S17 The infra-red images of IEG under different light intensity.

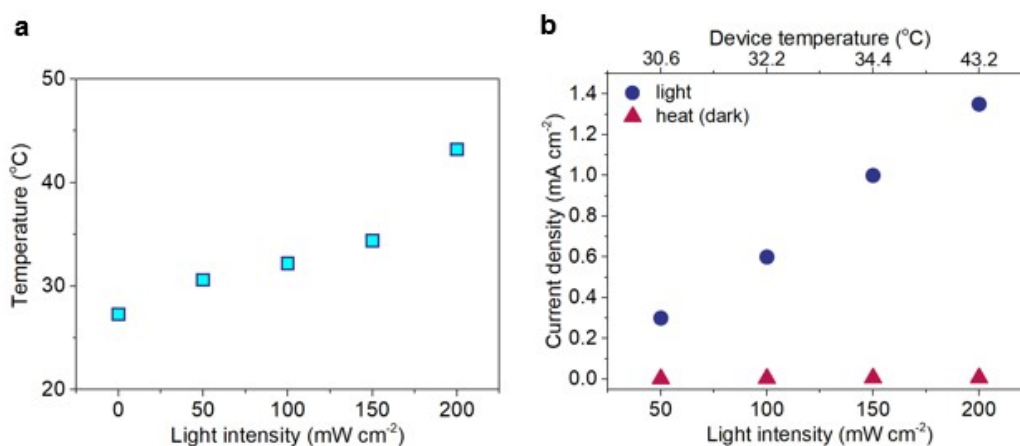


Fig. S18 (a) The device temperature of IEG under different light intensity. (b)  $I_{sc}$  of IEG under the same device temperature reaching by illumination or carbon fibers heating. These  $I_{sc}$  are obtained by subtracted current induced by moisture only from total  $I_{sc}$ .

Actually, illumination always arouse slight temperature rising of device owing to the photothermal effect,<sup>5</sup> which would further improve H<sup>+</sup> ion dissociation and diffusion.<sup>6</sup>

To verify the influence of photothermal effect in IEG, the upper electrode of IEG is heated to the same temperature using polyacrylonitrile-based carbon fibers directly.  $I_{sc}$  will slightly increase ( $0.007 \text{ mA cm}^{-2}$ ) but still lower than the  $I_{sc}$  of IEG induced by light when the device temperatures are the same ( $43 \text{ }^{\circ}\text{C}$ ). Therefore, the enhanced power generation under moisture companied with light would be derived from photoconductive effect rather than the photothermal effect.<sup>2,5,7</sup>

Table S2 The comparison information of different moist-electric generation systems with coordination of other environment energy source

Materials	Electrodes	Voltage (V)	Current density (mA cm <sup>-2</sup> )	Power density (μW cm <sup>-2</sup> )	Reference	
Graphene	g-GOF	Au	0.04	0.010	0.42	8
	IPMEG	rGO	0.18	0.001	0.10	9
	GO film-1	steel@Au	0.70	0.025	-	7
	GO film	Ag	0.70	0.003	27	10
	a-GOM	Au	0.45	0.001	0.0184	11
Other carbon-based materials	PCF	C	0.07	6E-7	-	13
	Cellulose	-	0.11	0.022	0.0003	14
	CNFs	copper	0.65	0.55	-	15
Polymer	PSSA	steel@Au	0.80	0.100	17	2
	PPy foam	Au	0.06	0.010	0.69	16
	HCl/ PVA	CNT	0.35	0.660	47	17
	PVA/GO	FTO	0.85	0.009	1.36	18
	GO/PAAS	Au/Ag	0.60	0.001	0.07	19
	PSSA+PVA	Ag NWs	0.60	0.100	7.9	20
	PSSA/PVA	carbon tape	0.95	0.001	5.5	21
	PSSA/R	Au	0.92	0.570	80	22
	PSSA-					
	PEDOT:PS S-FeCN <sup>4-/3-</sup>	graphite	0.94	0.840	72	23
Metallic oxide	TiO <sub>2</sub>	Ag NW	0.50	0.008	4	24
This work	PSSA-Kc	Au	0.8	1.6	88	

Table S3 The comparison information of different moist-electric generation systems without coordination of other environment energy source

Materials	Electrodes	Voltage (V)	Current density (mA cm <sup>-2</sup> )	Power density (μW cm <sup>-2</sup> )	Reference	
Graphene	g-GOF	Au	0.04	0.010	0.42	8
	IPMEG	rGO	0.18	0.001	0.10	9
	GO film-1	steel@Au	0.70	0.025	-	7
	GO film	Ag	0.70	0.003	27	10
	a-GOM	Au	0.45	0.001	0.0184	11
Other carbon-based materials	PCF	C	0.07	6E-7	-	13
	Cellulose	-	0.11	0.022	0.0003	14
	CNFs	copper	0.65	0.55	-	15
Polymer	PSSA	steel@Au	0.80	0.100	17	2
	PPy foam	Au	0.06	0.010	0.69	16
	HCl/ PVA	CNT	0.35	0.660	47	17
	PVA/GO	FTO	0.85	0.009	1.36	18
	GO/PAAS	Au/Ag	0.60	0.001	0.07	19
	PSSA+PVA	Ag NWs	0.60	0.100	7.9	20
	PSSA/PVA	carbon tape	0.95	0.001	5.5	21
	PSSA/R	Au	0.80	0.120	-	22
	PSSA- PEDOT:PS	graphite	0.85	0.150	5	23
	S-FeCN <sup>4-/3-</sup>					
Metallic oxide	TiO <sub>2</sub>	Ag NW	0.50	0.008	4	24
This work	PSSA-Kc	Au	0.60	0.250	6	

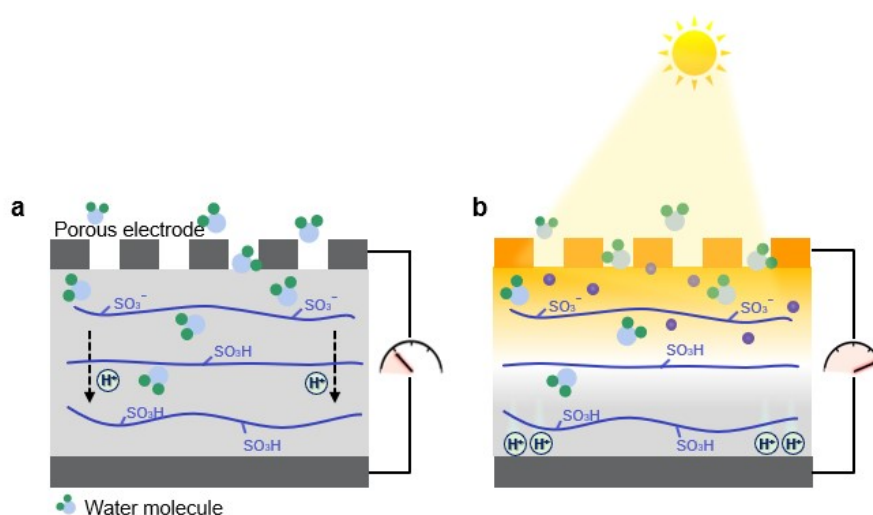


Fig. S19 (a) The functional groups in PSSA are ionized by incoming moisture and releases  $H^+$  ions. These free  $H^+$  ions move to the other side leaving negatively charged  $-SO_3^-$  groups. The positive/negative charge separation induces an electric field. (b) Kc in PSSA matrix are excited by illumination. Photogenerated carriers efficiently migrate under moisture-induced electric field, further enhancing  $I_{sc}$  output.

Table S4 Mass change of PSSA-Kc and i-PSSA-Kc film under different RH.

RH (%)	PSSA-Kc	i-PSSA-Kc
0.0	0.0	0.0
15.0	8.5	9.6
25.0	14.3	15.9
35.0	20.0	22.3
45.0	26.9	29.7
55.0	34.7	43.0
65.0	44.5	53.7
75.0	57.7	68.1
85.0	77.6	88.5
95.0	112.3	121.7

Dynamic vapor sorption (DVS) is an important quantitative method which can provide vast amounts of water sorption information over a wide RH range in real time, so it can be used to quantitatively analyze the water adsorption process.<sup>25</sup>

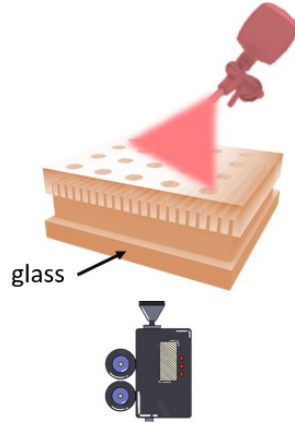


Fig. S20 Illustration of in situ monitoring water adsorption.

A camera can record the process of water molecule adsorption and migration in situ.

Table S5 Comparing information of coalescent water migration in IEG and planar structure device

	diagram	photograph	Contact area (mm <sup>2</sup> )	Diffusion velocity (mm s <sup>-1</sup> )
ME			78	0.1
Planar electrode			20	0.02

In order to observe water adsorption and migration process in a IEG in situ, by stacking a ME, PSSA-Kc film and a transparent substrate, a camera can record water wetting process beneath the device with planar structure or IAM structure. After water molecules spread along microgrooves on the ME, the microgrooves are filled so that the iridescence of ME disappears gradually. Obviously, adsorbed water could migrate to the covered region along microgrooves in the IEG based on IAM structure, which

results in more efficient electric generation.

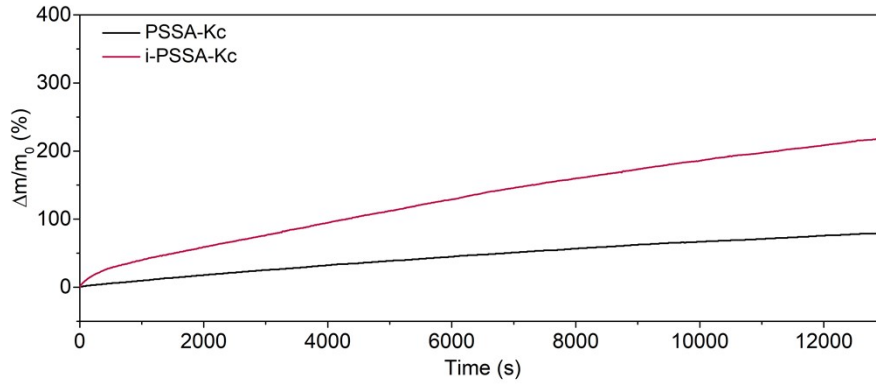


Fig. S21 The mass change of PSSA-Kc and i-PSSA-Kc film by water molecule adsorption versus time.

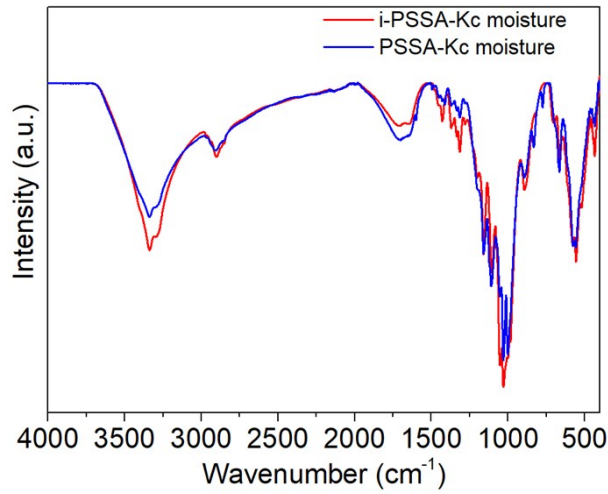


Fig. S22 FTIR curves of PSSA-Kc and i-PSSA-Kc film under RH = 70%.

The results of mass change, DVS and FTIR confirm that microgroove configuration plays an important role in water adsorption ability for enhanced power generation.

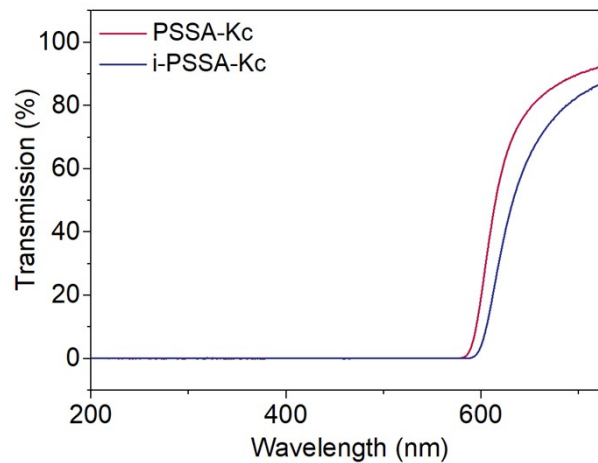


Fig. S23 Transmission spectra of PSSA-Kc and i-PSSA-Kc film.

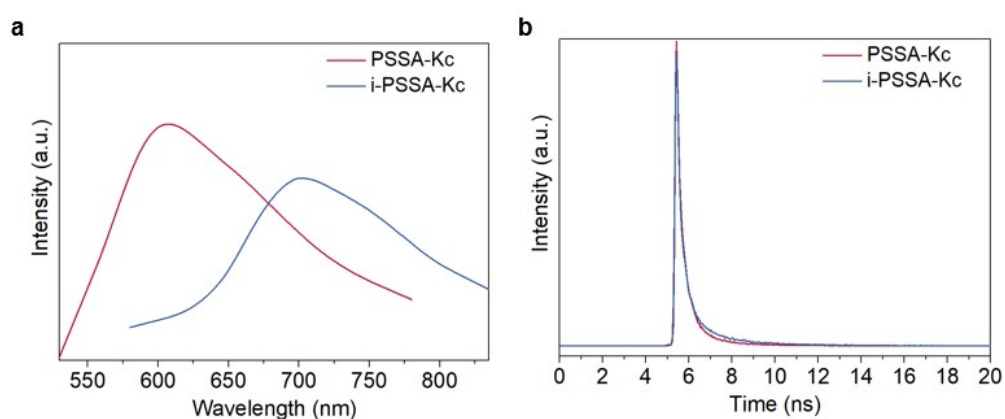


Fig. S24 (a) Steady state and (b) transient state photoluminescence (PL) spectra of PSSA-Kc film and i-PSSA-Kc film.

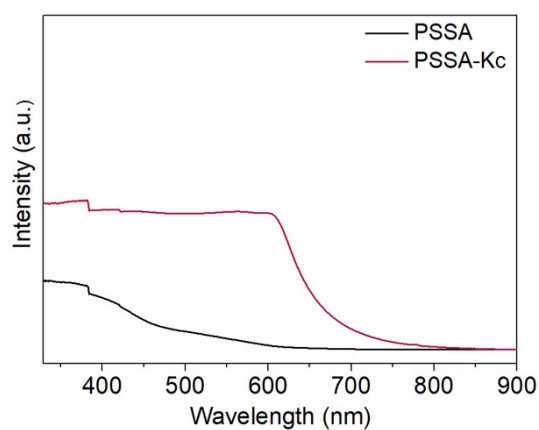


Fig. S25 UV-vis absorption curves of PSSA and PSSA-Kc film.

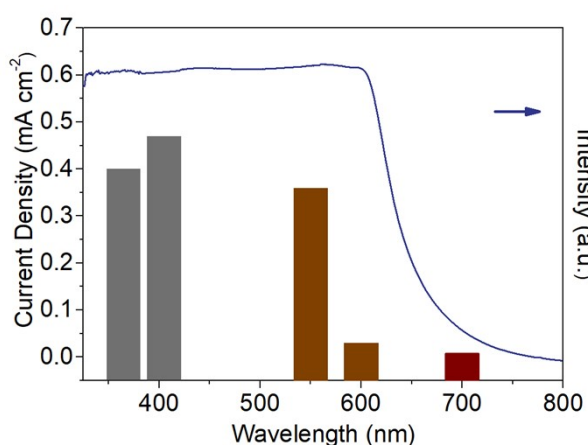


Fig. S26 Wavelength dependence of photocurrent and light absorption for an IEG. Photocurrent under single-wavelength illumination is tested under Xe lamp outfitted with the optical filters of 365 nm, 400 nm, 550 nm, 600 nm and 700 nm.

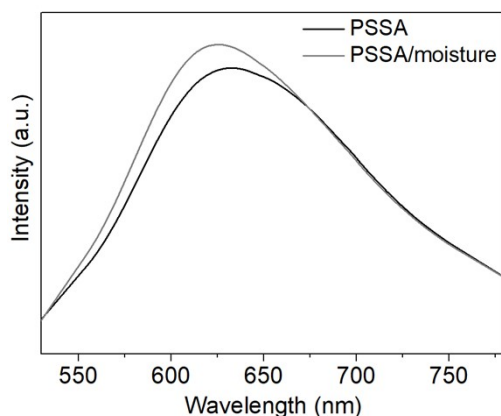


Fig. S27 PL spectra of original PSSA film and the film in RH of 70%.

Slight increased PL peaks in pure PSSA film after moisture adsorption indicates that strong photoluminescence quenching occurs in moisturized PSSA-Kc film caused by moisture-induced electric field rather than water adsorption.

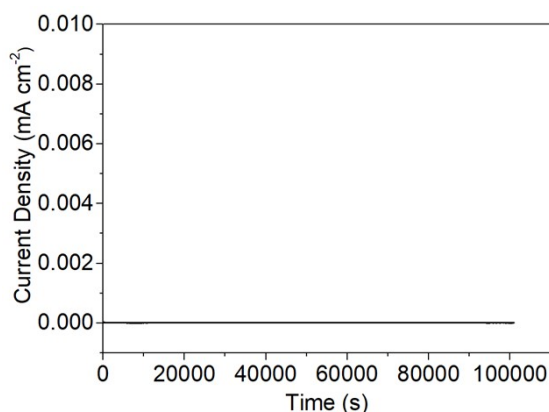


Fig. S28  $I_{sc}$  output of a IEG without moisture and illumination.

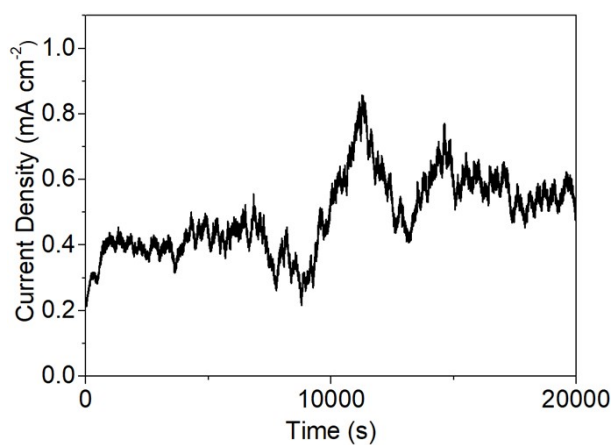


Fig. S29 The comparable  $I_{sc}$  of IEG in response to extra applied bias (0.53 V) under  $100 \text{ mW cm}^{-2}$  illumination without moisture.

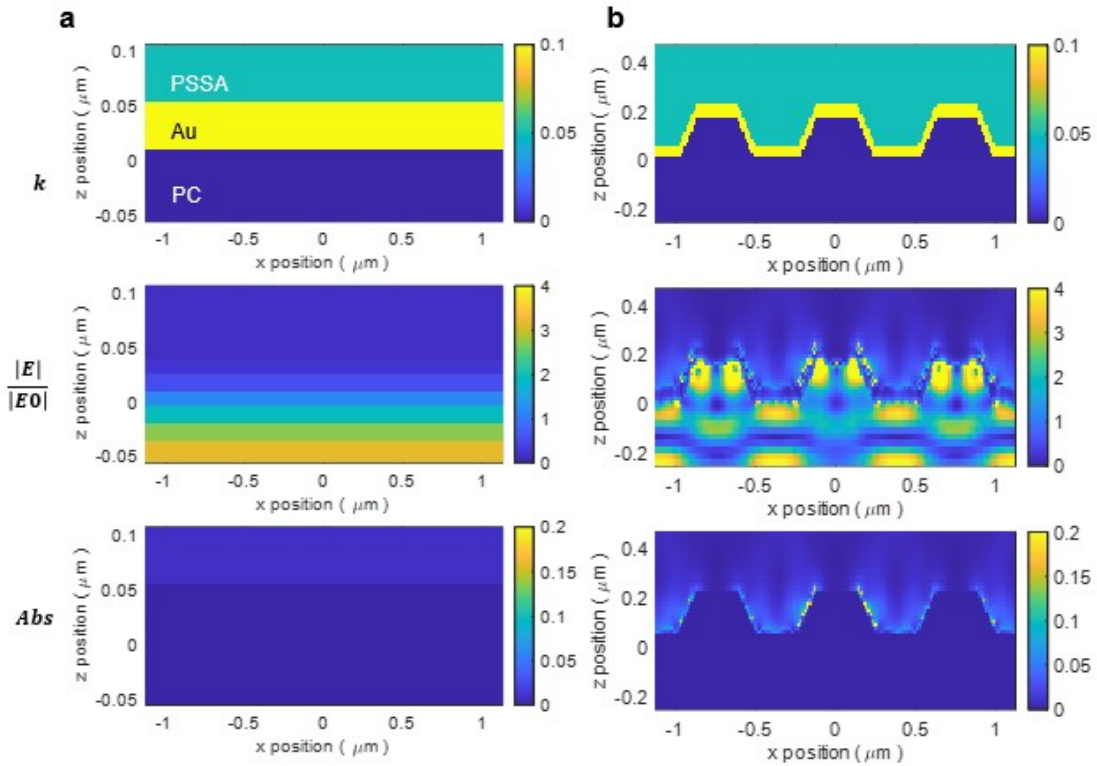


Fig. S30 Detailed structural parameters for FDTD simulation, field intensity distribution and absorption profile of IEG based on (a) planar interface structure or (b) IAM at 600 nm.

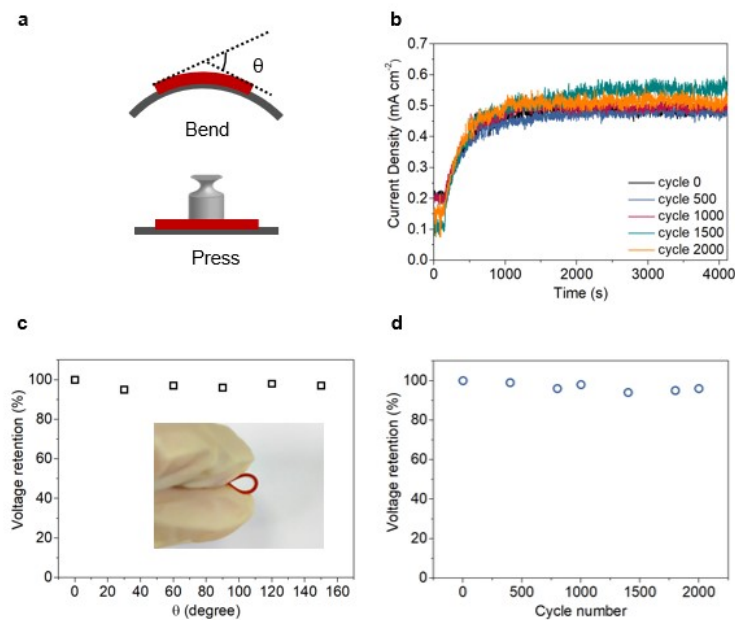


Fig. S31 The endurance of IEG undergoing mechanical deformations. (a) Schematic illustration under bending state and pressing state. (b)  $I_{sc}$  of IEG after various bending cycles at an angle of  $45^\circ$  under  $RH = 70\%$ . (c) Voltage retention of IEG under different bending angles at  $RH = 70\%$ . Insert: Photograph of the PSSA-Kc film under bending state. (d) Voltage retention of IEG after various pressing cycles of 2 N at  $RH = 70\%$ .

Based on the mechanical flexibility of PSSA-Kc film, the voltage output of IEG steadies under various bending angles from  $0^\circ$  to  $150^\circ$  at RH=70%. And the IEG retains about 100% of  $I_{sc}$  retention after 2000 cycles of bending  $45^\circ$ . The generated voltage of IEG still reaches to be about 0.74 V after 2000 pressing cycles of 2 N. Therefore, IEG viably exerts remarkable performance and stability under bending or pressing, implying its endurance for mechanical deformations.

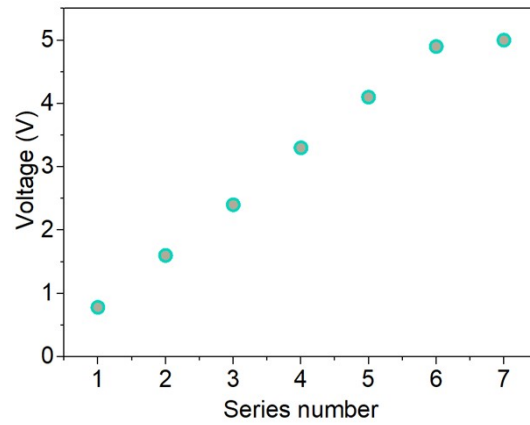


Fig. S32 The  $V_{oc}$  output of IEG units connected in series.

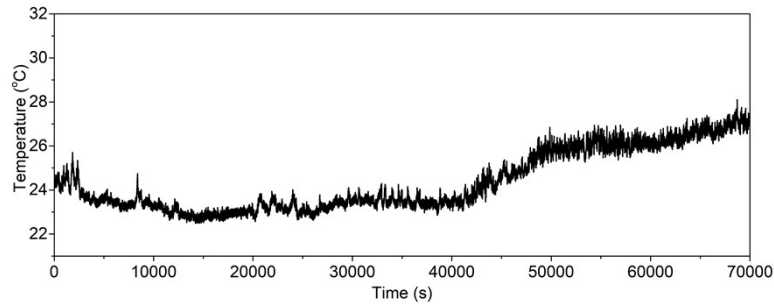


Fig. S33 The synchronous temperature variation when the performance of a IEG is test outdoors in Fig. 6c.

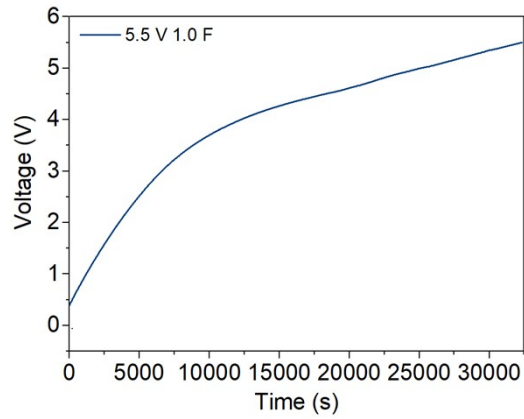


Fig. S34 Voltage-time curves of a commercial capacitor charged by 8 IEG units connected in series and parallel under natural condition.

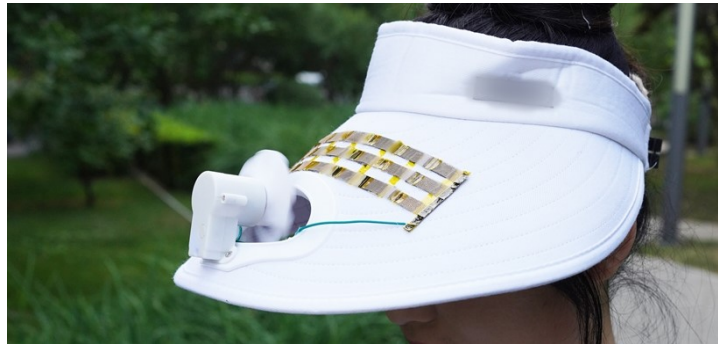


Fig. S35 IEGs are installed on the brim of a hat running an electric fan smoothly.



Fig. S36 IEGs assembled onto a windmill to serve as power supply system.

IEGs is capable of driving a detector to show air quality index including temperature, humidity, pollutant directly without any other auxiliaries

## Reference

1. A. Raman, Z. Yu and S. Fan, *Opt. Express*, 2011, **19**, 19015.
2. T. Xu, X. Ding, Y. Huang, C. Shao, L. Song, X. Gao, Z. Zhang and L. Qu, *Energy Environ. Sci.*, 2019, **12**, 972–978.
3. J. Bai, Y. Huang, H. Cheng and L. Qu, *Nanoscale*, 2019, **11**, 23083–23091.
4. Z. Wu, Y. Zhai, W. Yao, N. Eedugurala, S. Zhang, L. Huang, X. Gu, J. Ng and Y. Zhai, *Adv. Funct. Mater.*, 2018, **28**, 1805738.
5. J. Yang, X. Hu, X. Kong, P. Jia, D. Ji, D. Quan, L. Wang, Q. Wen, D. Lu and J. Wu, *Nat. Commun.*, 2019, **10**, 1171.
6. H. Tyrrell and R. Colledge, *Nature*, 1954, **173**, 264–265.
7. T. Xu, X. Ding, C. Shao, L. Song, T. Lin, X. Gao, J. Xue, Z. Zhang and L. Qu, *Small*, 2018, **14**, 1704473.
8. F. Zhao, H. Cheng, Z. Zhang, L. Jiang and L. Qu, *Adv. Mater.*, 2015, **27**, 4351–4357.
9. C. Yang, Y. Huang, H. Cheng, L. Jiang and L. Qu, *Adv. Mater.*, 2019, **31**, 1805705.
10. Y. Liang, F. Zhao, Z. Cheng, Y. Deng, Y. Xiao, H. Cheng, P. Zhang, Y. Huang, H. Shao and L. Qu, *Energy Environ. Sci.*, 2018, **11**, 1730–1735.
11. H. Cheng, Y. Huang, F. Zhao, C. Yang, P. Zhang, L. Jiang, G. Shi and L. Qu, *Energy Environ. Sci.*, 2018, **11**, 2839–2845.
12. Y. Huang, H. Cheng, C. Yang, P. Zhang, Q. Liao, H. Yao, G. Shi and L. Qu, *Nat. Commun.*, 2018, **9**, 4166.
13. K. Liu, P. Yang, S. Li, J. Li, T. Ding, G. Xue, Q. Chen, G. Feng and J. Zhou, *Angew. Chem. Int. Ed.*, 2016, **55**, 8003–8007.
14. M. Li, L. Zong, W. Yang, X. Li, J. You, X. Wu, Z. Li and C. Li, *Adv. Funct. Mater.*, 2019, **29**, 1901798.
15. J. Eun and S. Jeon, *Nano Energy*, 2022, **92**, 106772.
16. J. Xue, F. Zhao, C. Hu, Y. Zhao, H. Luo, L. Dai and L. Qu, *Adv. Funct. Mater.*, 2016, **26**, 8784–8792.
17. Z. Luo, C. Liu and S. Fan, *Nano Energy*, 2019, **60**, 371–376.
18. R. Zhu, Y. Zhu, F. Chen, R. Patterson, Y. Zhou, T. Wan, L. Hu, T. Wu, R. Joshi, M. Li, C. Cazorla, Y. Lu, Z. Han and D. Chu, *Nano Energy*, 2022, **94**, 106942.
19. Y. Huang, H. Cheng, C. Yang, H. Yao, C. Li and L. Qu, *Energy Environ. Sci.*, 2019, **12**, 1848–1856.
20. H. Wang, H. Cheng, Y. Huang, C. Yang, D. Wang, C. Li and L. Qu, *Nano Energy*, 2020, **67**, 104238.
21. H. Wang, Y. Sun, T. He, Y. Huang, H. Cheng, C. Li, D. Xie, P. Yang, Y. Zhang and L. Qu, *Nat. Nanotechnol.*, 2021, **16**, 811–819.
22. J. Bai, Y. Huang, H. Wang, T. Guang, Q. Liao, H. Cheng, S. Deng, Q. Li, Z. Shuai and L. Qu, *Adv. Mater.*, 2022, **34**, 2103897.
23. J. Bai, Y. Hu, T. Guang, K. Zhu, H. Wang, H. Cheng, F. Liu and L. Qu, *Energy Environ. Sci.*, 2022, **15**, 3086–3096.
24. D. Shen, M. Xiao, G. Zou, L. Liu, W. W. Duley and Y. N. Zhou, *Adv. Mater.*,

2018, **30**, 1705925.

25. M. J. Lundahl, A. G. Cunha, E. Rojo, A. C. Papageorgiou, L. Rautkari, J. C. Arboleda and O. J. Rojas, *Sci. Rep.*, 2016, **6**, 30695.